Enhanced interfacial charge transport motivated by Bi_2Te_3-$SbPO_4$@NC heterointerface for superior Zn^{2+} and NH_4^+ storage system

Zhiyuan Zha,[a] Ruinan Chen,[a] *Tong Zhou,*[b,d*] Daohong Zhang,[*a,c] Qiufan Wang[*a,c]

[a] Key Laboratory of Catalysis and Energy Materials Chemistry of Ministry of Education & Hubei Key Laboratory of Catalysis and Materials Science, Hubei R&D Center of Hyperbranched Polymers Synthesis and Applications, South-Central Minzu University, Wuhan 430074, China

[b] Hubei Key Laboratory of Energy Storage and Power Battery, School of New Energy, Hubei University of Automotive Technology, Shiyan 442002, China

[c] Guangdong Provincial Laboratory of Chemistry and Fine Chemical Engineering Jieyang Center, Jieyang 515200, China

[d] Key Laboratory of Advanced Energy Materials Chemistry, Nankai University, Tianjin 300071, China

Email: daohong.zhang@scuec.edu.cn (D. Zhang); ygdf@mail.scuec.edu.cn (Q. Wang)

1. Experimental section

Synthesis of Bi-MOF: 450 mg of 1,3,5-benzenetricarboxylic acid, 90 mg of $Bi(NO_3)_3 \cdot 5H_2O$ were added to a 60 mL methanol solution. After ultrasonic dissolution, it was transferred to a high-pressure reactor and reacted in an oven at 120 °C for 24 hours. The white powder Bi-MOF was obtained by centrifugation, washing three times with methanol, and drying in an oven at 80 °C for 8 hours.

Synthesis of Bi_2Te_3@NC: The as-prepared Bi-MOF and Te powder with the mass ratio of 2:1 were placed at the downstream and upstream position of porcelain boat in the tube furnace, then heat to 600 °C at a rate of 10 °C/min and kept for 3 h under Ar atmosphere to yield Bi_2Te_3@NC.

Synthesis of Bi_2Te_3-$SbPO_4$@NC: Bi_2Te_3@NC powder (0.2 mmol , $SbCl_3$ (0.1 mmol) and $NH_4H_2PO_4$ (0.1 mmol) were added into 30 ml ethylene glycol solution. After stirring for 3 h, the solution was transferred to a 100ml autoclave. After reaction at 180 °C for 4 h, the product was rinsed with water and ethanol for three times respectively. After drying in an 80 °C oven for 8 h, the black Bi_2Te_3-$SbPO_4$@NC powder was obtained.

Materials and Methods:

Synthesis of Zn@ZnF_2: 2.5 mmol of SnF_2 was dissolved in 100 ml of deionized water, and the Zn foil was soaked in it for 3 min. After drying in a 60 °C oven for 4 h, Zn@ZnF_2 was obtained.

Characterization

The synthesized samples were characterized by X-ray powder diffraction (XRD), X-ray photoelectron spectroscopy (XPS). The morphology and structure of the samples were characterized by scanning electron microscopy (SEM) and transmission electron microscopy (TEM).

Electrochemical measurements

The material, Super P and polyvinylidene fluoride were mixed in N-methylpyridinone solvent at a mass ratio of 7:2:1, and then the slurry was coated on the carbon cloth and vacuum dried at 60 ° for 12 h. The loading mass of active material is about 1.0~1.5 mg cm^{-2}. The electrochemical evaluation was carried out by assembling into a CR2032-

type coin cell, using Zn@ZnF_2 and non-woven filter paper as the anode and separator, respectively, 2 M $ZnSO_4$ as the electrolyte. Cyclic voltammetry (CV) measurements were carried out on an electrochemical workstation (Ivium, CompactState 10800). Electrochemical impedance spectra (EIS) was recorded on a CHI760 electrochemical workstation (Shanghai Chenhua, China). The galvanostatic charge/discharge (GCD) measurements of the coin cells were measured utilizing Neware battery tester (BTS-4000) in a potential range of 0.1~1.6 V (vs Zn^{2+}/Zn). The electrochemical performance of the AIB was tested by IVium. In terms of single electrode performance, Bi_2Te_3@NC and Bi_2Te_3-$SbPO_4$@NC were used as working electrodes, carbon rod was used as counter electrode, saturated calomel electrode (SCE) was used as reference electrode, and a three-electrode structure electrode was constructed in 15 M CH_3COONH_4 electrolyte aqueous solution. Finally, the electrochemical performance of Bi_2Te_3-$SbPO_4$@NC was studied by using 15 M CH_3COONH_4+2 M $ZnSO_4$ as the electrolyte of mixed ion battery.

Detail of calculation

(1) Capacitance contribution

the measure current (i) and scan rate (v) in CV curves have relationships with equation:

$$i=a^v b \quad (1)$$

$$logi=blogv+loga \quad (2)$$

Where a denotes a constant, b is equal to the slope of lgv-lgi plots, i represents peak current, v is the scan rate of CV curve. When the value of b is close to 0.5, the electrode shows a diffusion process, and when the value of b is close to 1, the capacitance process is dominant.

Capacitance contribution can be further calculated according to the equations:

$$i(v)=k_1v+k_2v^{1/2} \quad (3)$$

$$i(v)/v^{1/2}=k_1v^{1/2}+k_2 \quad (4)$$

Where k_1 value was obtained from the slope of linear fit of the $i/v^{1/2}$ versus $v^{1/2}$ plot. The capacitive and diffusion-controlled contributions were obtained by k_1v and $k_2v^{1/2}$, respectively.

(2) Galvanostatic current intermittent titration technique (GITT)

GITT is used to measure the diffusion coefficient of Zn^{2+} in zinc ion battery and NH_4^+ in a three-electrode system. The diffusion coefficient can be obtained according to the following equation:

$$D=(4L^2/\pi\tau)(\Delta E_s/E_\tau)^2 \quad (5)$$

Where τ(s) is the constant current pulse time. L corresponds to NH_4^+ diffusion length, which is equal to thickness of the electrode. ΔE_s is the steady-state voltage change caused by current pulse. ΔE_τ is the voltage change during the constant current pulse.

Computational details:

All calculations were carried out for the material in the framework of Density Functional Theory (DFT) using the Vienna Ab initio Simulation Package (VASP 6.3.0).[1-3] The generalised gradient approximation (GGA) of the Perdew-Burke-Ernzerhof (PBE) function was used to describe the exchange-correlation energy.[4] The projected augmented wave (PAW) method and pseudopotentials were used to describe the interactions between valence electrons and ions.[5] To ensure the efficiency of the computational results and parallel computing. A 2×2×1 k-point grid under Monkhorst-Pack is used in the optimisation process and 450 eV truncation energy is set. The lattice parameters and ionic positions of all crystals were fully relaxed, and the convergence criteria for the total energy of all relaxed atoms and the final force were 10^{-5} eV and 0.03 eV/Å, respectively.

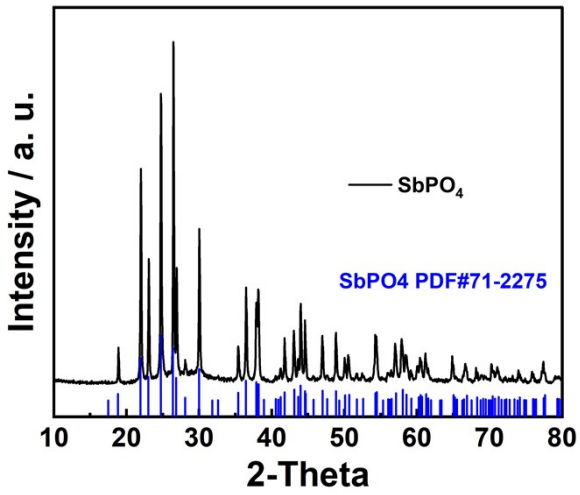

Figure S1. XRD pattern of $SbPO_4$.

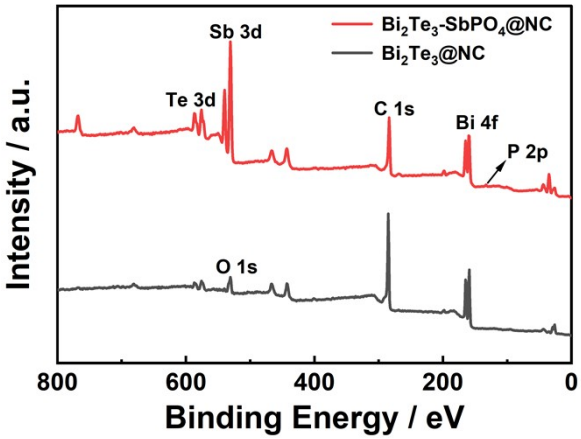

Figure S2. Total spectrum of *ex-situ* XPS of Bi_2Te_3 and Bi_2Te_3-$SbPO_4$@NC.

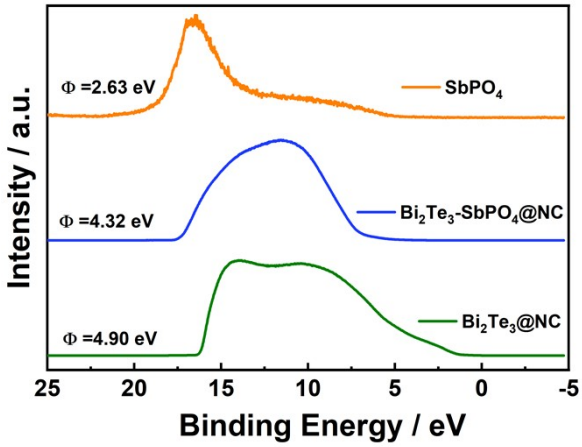

Figure S3. UPS valance band spectra of the samples.

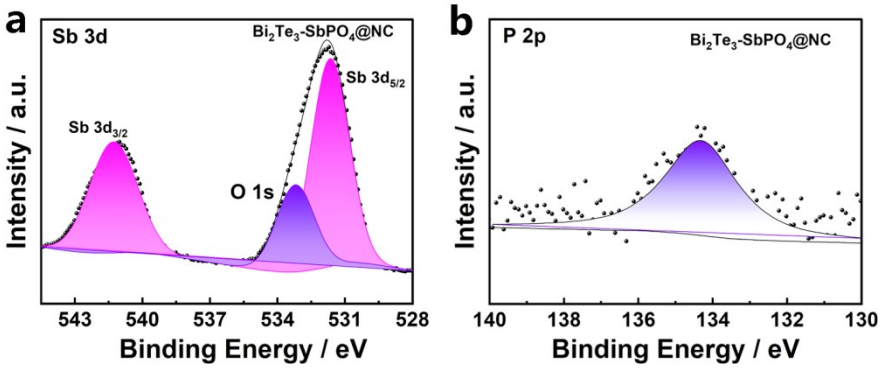

Figure S4. XPS spectra of (a) Sb 3d and (b) P 2p.

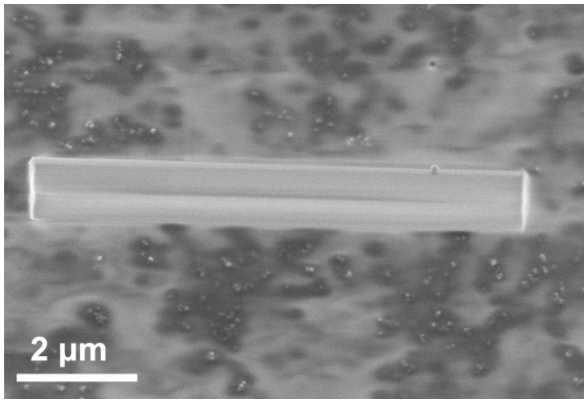

Figure S5. The SEM image of Bi-BTC.

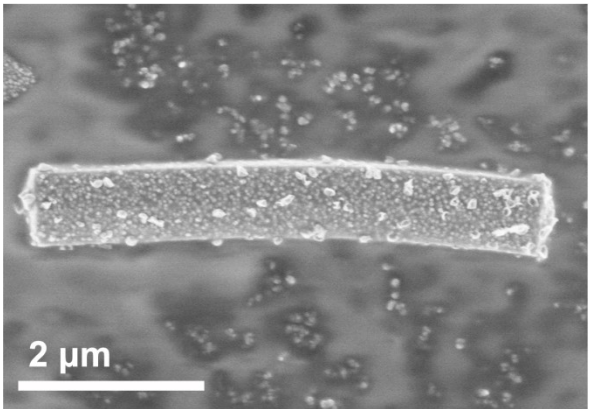

Figure S6. The SEM image of Bi_2Te_3@NC.

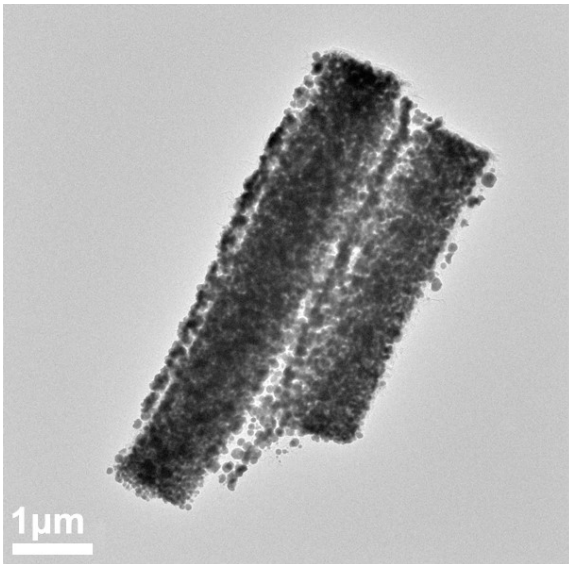

Figure S7. The TEM image of Bi_2Te_3@NC.

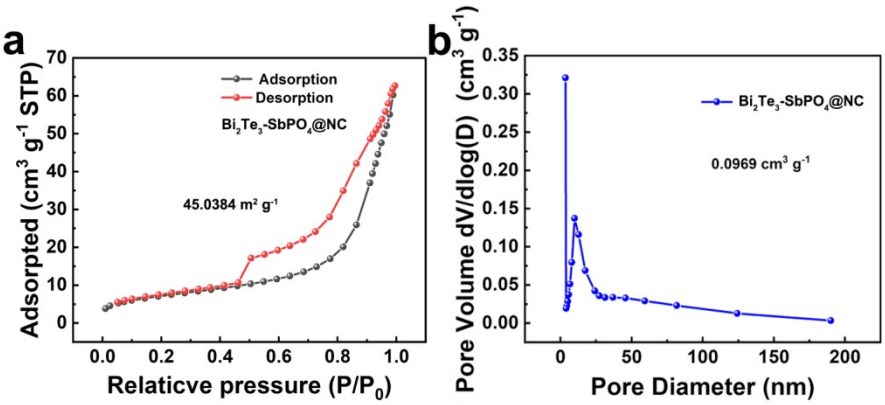

Figure S8. (a) Brunauer-Emmett-Teller (BET) curves of Bi_2Te_3-$SbPO_4$@NC. (b) The pore diameter distribution of Bi_2Te_3-$SbPO_4$@NC.

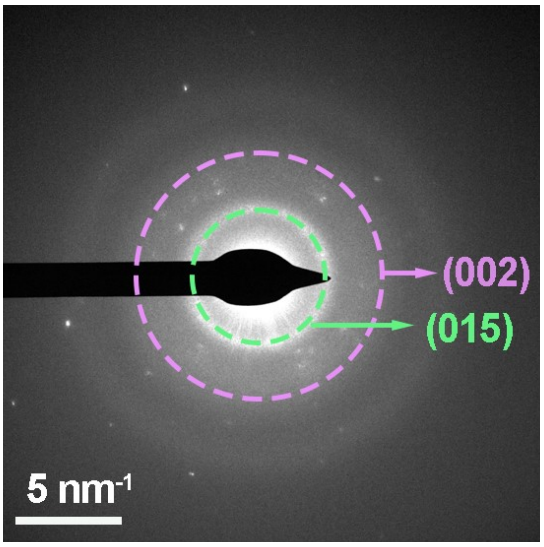

Figure S9. SAED pattern of Bi_2Te_3-$SbPO_4$@NC.

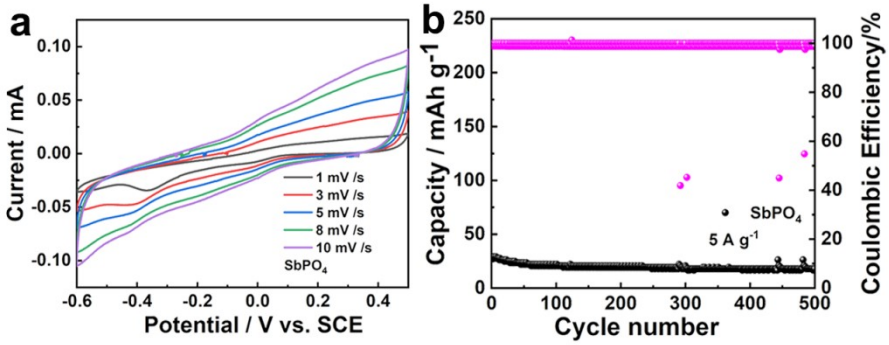

Figure S10. (a) The CV curves of $SbPO_4$ electrode at 15 M CH_3COONH_4 as electrolyte. (b) Cycling performance of $SbPO_4$ electrode at 2 M $ZnSO_4$ as electrolyte.

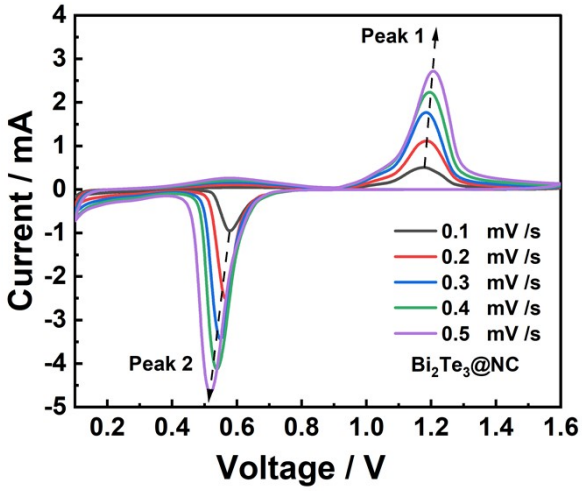

Figure S11. The CV curves of Bi_2Te_3@NC electrode at different scan rates of 0.1~0.5 mV s^{-1}.

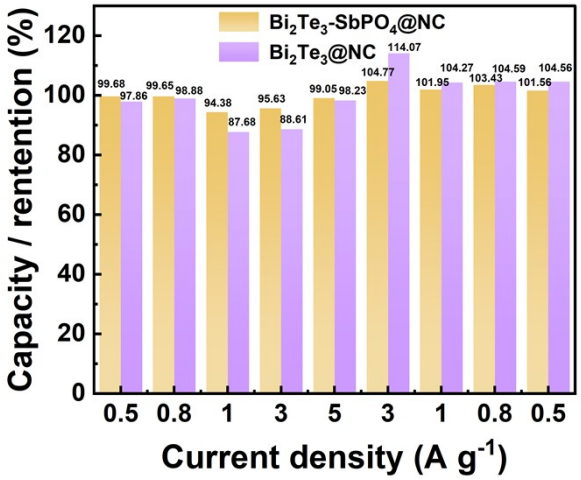

Figure S12. Capacity of the samples at different current densities ranging from 0.5 A g^{-1} to 5 A g^{-1}.

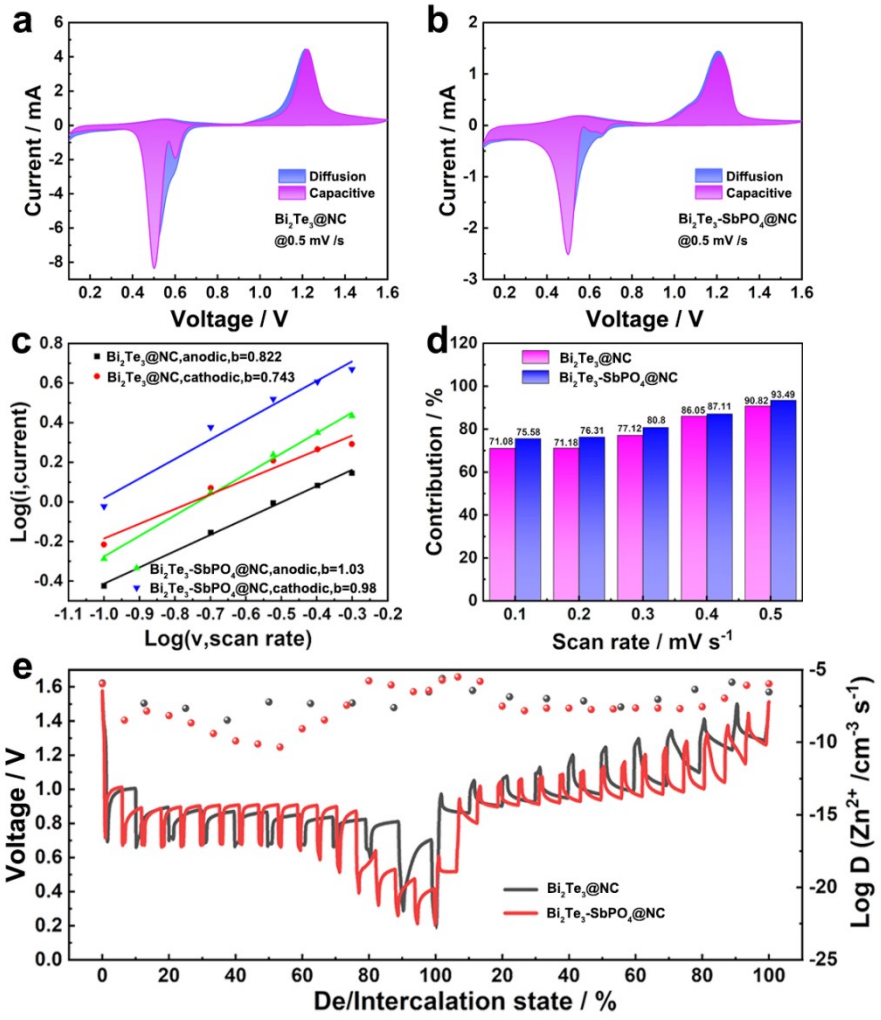

Figure S13. The capacitance contribution of (a) Bi_2Te_3@NC and (b) Bi_2Te_3-$SbPO_4$@NC at 0.5 mV s^{-1}. (c) Log *i versus* Log *v* plots and *b*-value determination. (d) The proportions of capacitive contribution at various scan rates for Bi_2Te_3@NC and Bi_2Te_3-$SbPO_4$@NC. (e) GITT curves and *D* values for Bi_2Te_3@NC and Bi_2Te_3-$SbPO_4$@NC.

The kinetic properties of Bi_2Te_3@NC and Bi_2Te_3-$SbPO_4$@NC were tested. For the Bi_2Te_3-$SbPO_4$@NC heterojunction, the calculated *b* values are 1.03 and 0.98, respectively, indicating that it is mainly a capaciticance-controlled behavior. In contrast, the *b* values of pure Bi_2Te_3@NC are 0.822 and 0.743, respectively (Figure S13c), indicating that the storage reaction is controlled by both diffusion control and capacitance control. In addition, at different CV scan rates, the capacitive contribution ratio of Bi_2Te_3-$SbPO_4$@NC heterojunction is higher than that of Bi_2Te_3@NC (Figure

S13a-b and S13d), confirming faster ion storage kinetics. The ion diffusion coefficient of Bi_2Te_3-$SbPO_4$@NC was quantitatively evaluated by constant current intermittent titration technique (GITT). The ion diffusion coefficient of Bi_2Te_3-$SbPO_4$@NC was about 10^{-10}~10^{-5} cm^2 s^{-1} (Figure S13e), indicating that the built-in electric field promoted the enhancement of charge transfer.

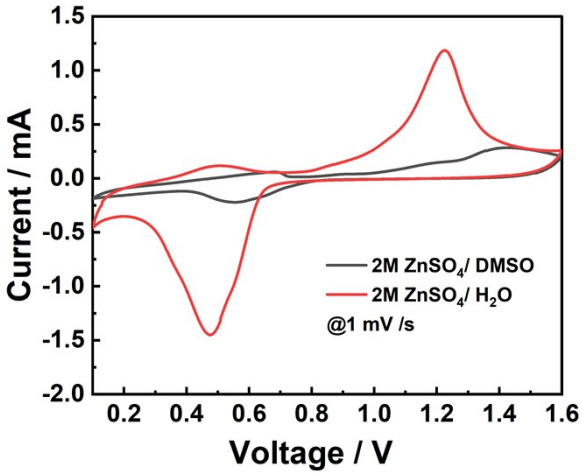

Figure S14. CV curve of Bi_2Te_3-$SbPO_4$@NC at 1 mV s^{-1} in 2 M $ZnSO_4/H_2O$ and 2 M $ZnSO_4$/DMSO solution.

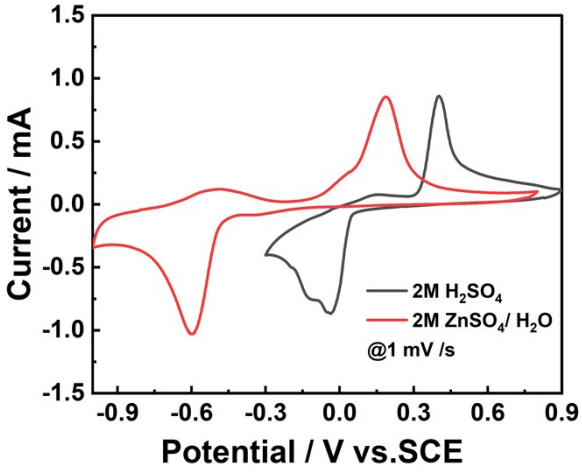

Figure S15.CV curve of Bi_2Te_3-$SbPO_4$@NC at 1 mV s^{-1} in 2 M H_2SO_4 and 2 M $ZnSO_4/H_2O$ solution.

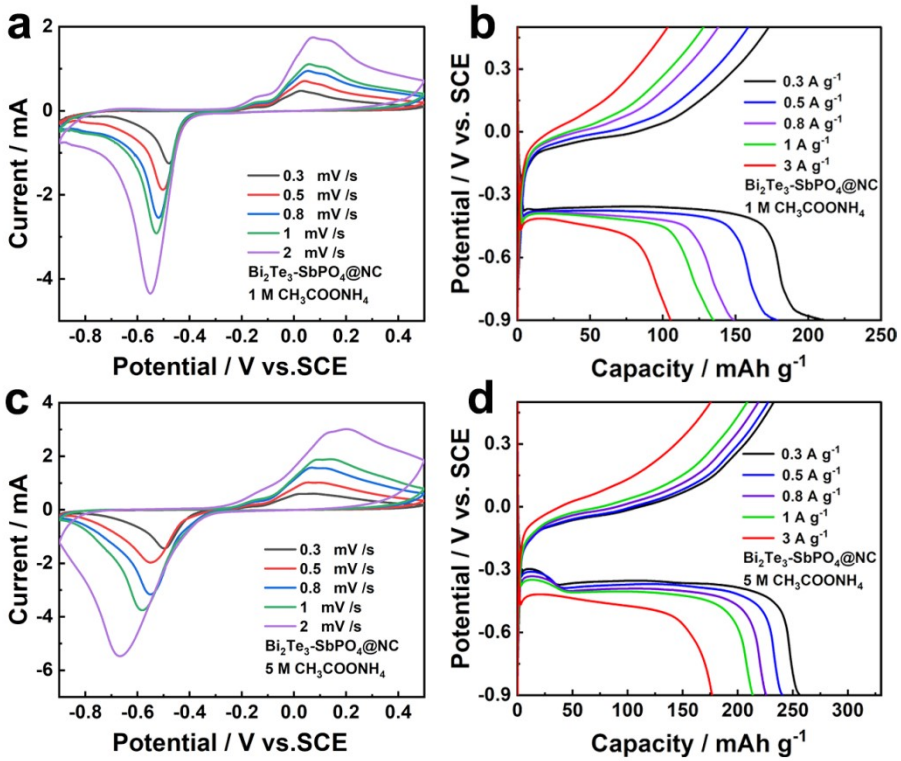

Figure S16. (a,b) Electrochemical properties of Bi_2Te_3-$SbPO_4$@NC at 1 M CH_3COONH_4 as electrolyte. (c,d) Electrochemical properties of Bi_2Te_3-$SbPO_4$@NC at 5 M CH_3COONH_4 as electrolyte.

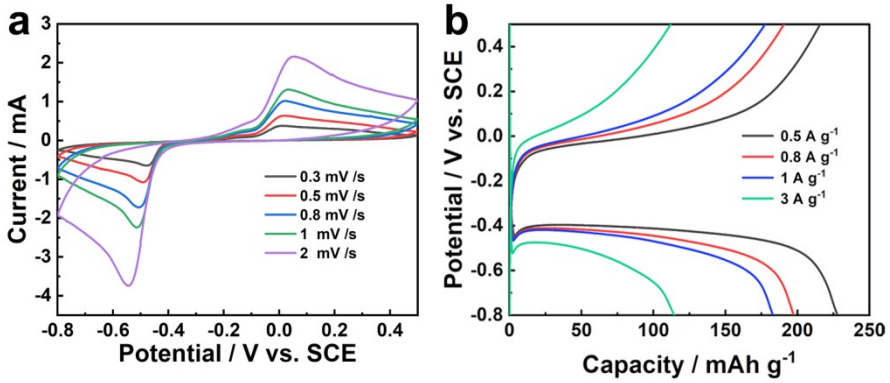

Figure S17. Electrochemical properties of Bi_2Te_3@NC.

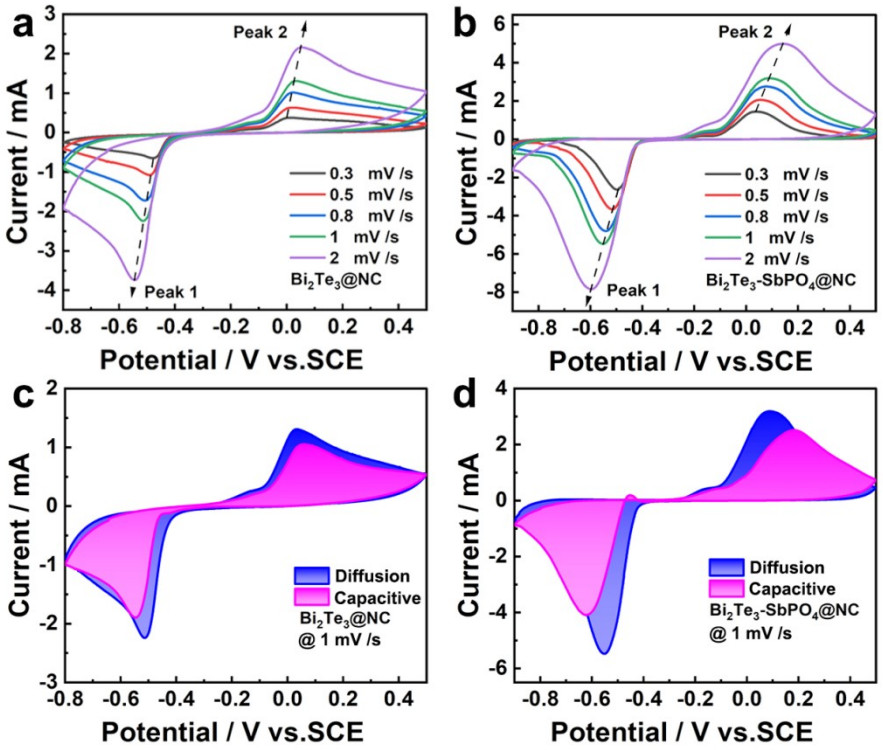

Figure S18. The CV curves of (a) Bi_2Te_3@NC and (b) Bi_2Te_3-$SbPO_4$@NC electrode at different scan rates of 0.3~2 mV s^{-1}. The capacitance contribution of (c) Bi_2Te_3@NC and (d) Bi_2Te_3-$SbPO_4$@NC at 1 mV s^{-1}.

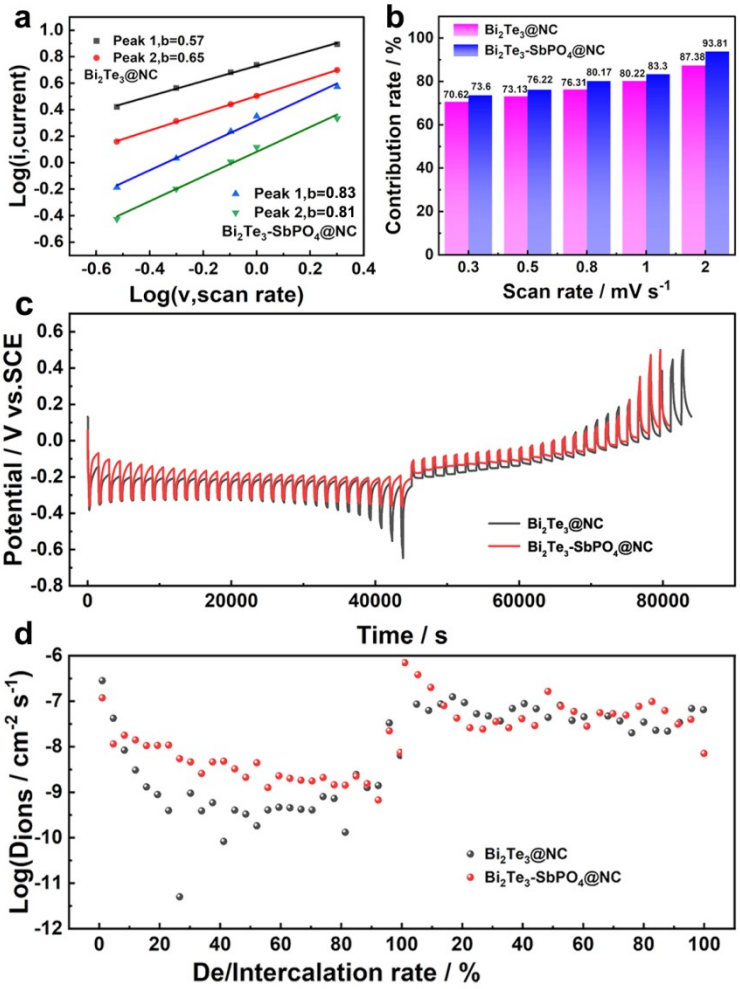

Figure S19. (a) Log *i versus* Log *v* plots and b-value determination. (b) The proportions of capacitive contribution at various scan rates for Bi_2Te_3@NC and Bi_2Te_3-$SbPO_4$@NC. (c) GITT curves and (d) D values for Bi_2Te_3@NC and Bi_2Te_3-$SbPO_4$@NC.

CV tests were performed on Bi_2Te_3@NC and Bi_2Te_3-$SbPO_4$@NC at a scan rate of 0.3~2 mV s^{-1} (Figure S18a-b). For the Bi_2Te_3-$SbPO_4$@NC heterojunction electrode, the b values were measured to be 0.83 and 0.81, respectively, indicating that the storage reaction is controlled by both diffusion control and capacitance control (Figure S19a). The b values of Bi_2Te_3@NC pure materials are 0.57 and 0.65, and the storage reaction is also controlled by capacitance and diffusion. The capacitance contribution rates of the two groups of materials at different scanning rates were calculated (Figure S19b). It is found that the contribution of capacitance increases with the increase of scanning rate. At 1 mV s^{-1}, the contribution rate of pseudocapacitance of Bi_2Te_3-$SbPO_4$@NC is 83.3 % (Figure S18c), while the contribution rate of pseudocapacitance of Bi_2Te_3@NC

is 80.22 % (Figure S18d). The capacitance contribution ratio of Bi_2Te_3-$SbPO_4$@NC heterojunction is higher than that of Bi_2Te_3@NC, which confirms the faster reaction kinetics. The ion diffusion coefficients of Bi_2Te_3-$SbPO_4$@NC and Bi_2Te_3@NC were determined by a constant current intermittent titration technique (GITT) at 0.1 A g^{-1} (Figure S19c). It is calculated that the NH_4^+ ion diffusion coefficient of the Bi_2Te_3-$SbPO_4$@NC heterojunction electrode is 10^{-9}~10^{-6} cm^2 s^{-1}, while the NH_4^+ diffusion coefficient of the Bi_2Te_3@NC electrode is 10^{-10}~10^{-6} cm^2 s^{-1} (Figure S19d). The results further prove that the Bi_2Te_3-$SbPO_4$@NC electrode has a faster ion diffusion rate in the NH_4^+ storage system.

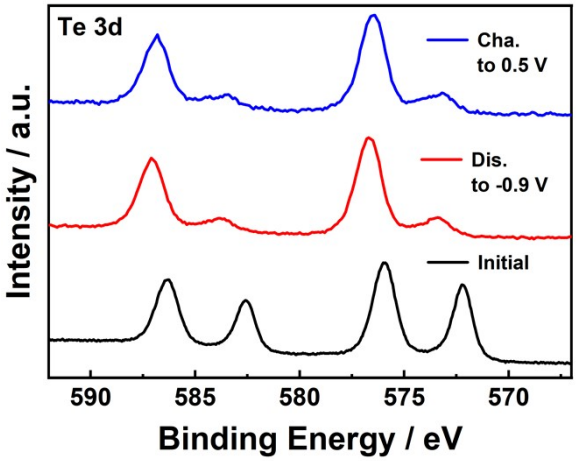

Figure S20. XPS spectra of Te 3d.

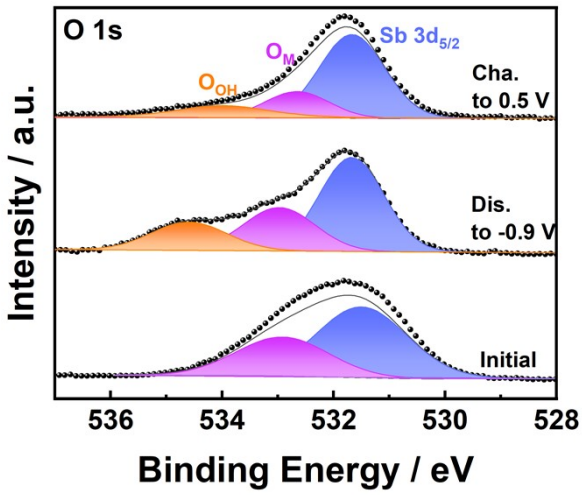

Figure S21. XPS spectra of O 1s.

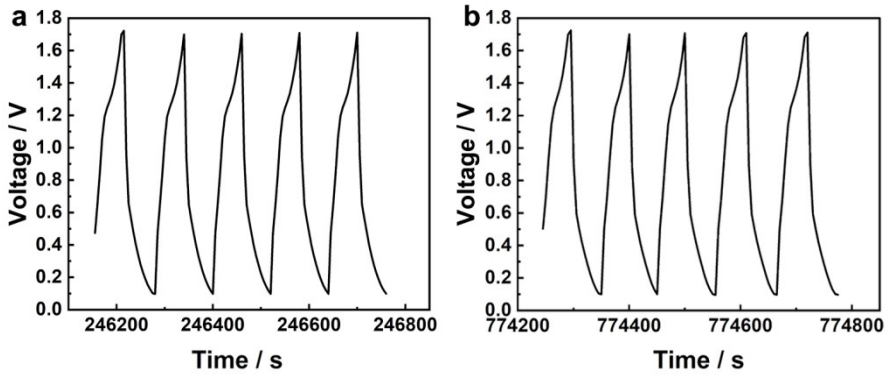

Figure S22. The charge and discharge curves of Bi_2Te_3-$SbPO_4$@NC at the 2000-2005th cycle (a) and the 6000-6005th cycle (b).

References：

[1] University of Vienna, Vienna Ab initio Simulation Package (VASP 6.2.0), 2020, https://www.vasp.at/.

[2] G. Kresse and J. Furthüller, Efficient iterative schemes for ab initio total-energy calculations using a plane-wave basis set, Phys. Rev. B, 1996, 54, 11169-11186.

[3] G. Kresse and D. Joubert, From ultrasoft pseudopotentials to the projector augmented-wave method, Phys. Rev. B, 1999, 59, 1758-1775.

[4] J. P. Perdew, K. Burke and M. Ernzerhof, Generalized gradient approximation made simple, Phys. Rev. Lett., 1996, 77, 3865-3868.

[5] P. E. Blöchl, Projector augmented-wave method, Phys. Rev. B, 1994, 50, 17953-17979.